

Magnetoelasticity in MnPt $L1_0$ system

Jakub Šebesta,^{1,*} Michal Vališka,² Karol Synoradzki,³ Tamara J. Bednarchuk,⁴ and Dominik Legut^{2,1,†}

¹*IT4Innovations, VSB – Technical University of Ostrava,
17. listopadu 2172/15, 708 00 Ostrava, Czech Republic*

²*Charles University, Faculty of Mathematics and Physics Ke Karlovu 3, 121 16 Praha 2, Czech Republic*

³*Institute of Molecular Physics, Polish Academy of Sciences, Smoluchowskiego 17, 60-179 Poznań, Poland*

⁴*Institute of Low Temperature and Structure Research,
Polish Academy of Sciences, Okólna 2, 50-422 Wrocław, Poland*

(Dated: March 20, 2025)

Magnetic materials play an important role in the industry. Except for common material parameters such as magnetocrystalline anisotropy, magnetoelastic behavior can be significant for application serving in various devices, e.g. in acoustic actuators, transducers, or sensors providing desirable fast response and high efficiency. Magnetoelastic properties have been studied for the cubic system. However, their magnetoelastic behavior is weak. Therefore, we focus on Pt-based tetragonal binary compounds bearing engaging magnetic behavior. We evaluate MnPt magnetoelastic behavior using the finite displacement method, discussing the influence of the magnetic structure, and focusing on the origin. While, the theoretically obtained results are compared to our performed experiments.

I. INTRODUCTION

The mechanical properties of the material are important for practical application. Nevertheless, for magnetic materials, high complexity emerges due to the coupling of magnetic and elastic properties giving rise to the so-called magnetoelastic behavior [1]. There exist various kinds of magnetoelastic effect, e.g. magnetostriction, magnetovolume effect, or Wiedemann effect, bringing many useful applications. Thus, magnetoelasticity can take place in force sensors, low-frequency weak field detectors, fast pulse generators, rotational and linear motors or magneto-acoustically driven low-energy demanding electronics [2–6]. Magnetoelasticity arises from various energy contributions such as magnetocrystalline anisotropy (MCA), magnetic exchange interactions, and dipole interaction. In the present work, we focus on the influence of the magnetic ordering structure of MnPt system on its magnetoelastic properties. Magnetoelastic behavior, which stem from an interplay between the magnetic and elastic properties substantially differing among the magnetic compounds. The MnPt might bear interesting properties as it belongs to the family of Pt-based tetragonal systems possessing a large MCA [7]. It comes from the interplay of Pt strong spin-orbit coupling (SOC) with large spin magnetic moments of the 3d-elements. At room temperature, MnPt forms the $L1_0$ phase. It was found that such an Mn-based two component alloy possesses surprisingly high Néel temperature (MnPt $T_N > 900$ K) [8]. The antiferromagnetic ordering of Mn-based systems arises from around half-filled Mn d-states [9]. The antiferromagnetic magnetic structure of MnPt is characterized by [001] Néel vector. With elevated temperature, a spin-flip occurs (580 K–770 K) [10]

turning the spin orientation toward the [100] direction. MnPt magnetic properties are useful for spin-valve structures with giant magnetoresistance as a pinning layer or in tunnel magnetoresistance devices. Besides, the MnPt a lattice parameter is close to the Fe or MgO ones, which makes MnPt interesting for making interfaces.

This work study the impact of different magnetic structures to the magnetoelastic behavior by studying changes in magnetoelastic and magnetoelastic properties based on ab-initio calculations. It reveals a huge modification of the magnetoelasticity with respect to the considered magnetic structure. The analysis also includes probing the origin of the observed changes. To prove obtained ground state results, the magnetostictive behavior was experimentally measured on a polycrystalline sample.

The paper is organized as follows. Initially, theory and calculations' resp. experimental details are stated. Further, the structure and magnetic properties of the selected magnetic structures are determined and compared with measurements performed on the prepared polycrystalline sample. In order to study the magnetoelastic properties, the elastic constants are estimated. Then, anisotropic magnetoelastic behavior is studied. The magnetoelastic constants and magnetoelastics are evaluated and compared to the experimental measurements. The origin of the differences between the considered magnetic structures is discussed on the basis of orbital-resolved magnetocrystalline anisotropy energy (MAE) contributions and induced changes of the charge densities. Later, the isotropic volume change is estimated, including calculation of magnetic exchange interactions. Finally, conclusions are provided.

* jakub.sebesta@vsb.cz

† dominik.legut@vsb.cz

II. METHODOLOGY

A. Theory

Magnetostriction describes the deformation of the material dimensions in response to magnetism. It has two contributions, the anisotropic magnetostriction originating from dependence of magnetocrystalline anisotropy and the isotropic volume one based on the isotropic exchange interaction.

Small deformations in solids are described by a strain tensor [11]

$$\varepsilon_{ij} = \left(\frac{\partial u_i}{\partial r_j} + \frac{\partial u_j}{\partial r_i} \right), \quad (1)$$

where $\mathbf{u}(r) = \mathbf{r}' - \mathbf{r}$ denotes a displacement vector. The magnetostriction can be expressed by the magnetization given change of the length of a originally demagnetized material [12, 13]

$$\frac{l - l_0}{l} \Big|_{\boldsymbol{\beta}}^{\boldsymbol{\alpha}} = \sum_{i,j=x,y,z} \varepsilon_{ij}^{eq} \beta_i \beta_j, \quad (2)$$

where l_0 denotes the length along the $\boldsymbol{\beta}$ direction of a demagnetized sample and l is the length in the same direction when the sample is magnetized along the $\boldsymbol{\alpha}$ direction. The equilibrium strain tensor ε_{ij}^{eq} comes from minimization of the elastic energy E_{el} and magnetoelastic energy E_{me} with the strain [1, 14, 15]

$$\frac{\partial E_{el} + E_{me}}{\partial \varepsilon_{ij}^{eq}} = 0. \quad (3)$$

Regarding the studied MnPt systems bearing the symmetry of the tetragonal (I) system, the elastic energy has the following form in the Cartesian axes [16],

$$\begin{aligned} \frac{1}{V_0} (E_{el} - E_0) = & \quad (4) \\ & \frac{1}{2} C_{11} (\varepsilon_1^2 + \varepsilon_2^2) + C_{12} \varepsilon_1 \varepsilon_2 + C_{13} (\varepsilon_1 + \varepsilon_2) \varepsilon_3 \\ & + \frac{1}{2} C_{33} \varepsilon_3^2 + \frac{1}{2} C_{44} \varepsilon_4^2 + \varepsilon_5^2 + \frac{1}{2} C_{66} \varepsilon_6 \\ & = \frac{1}{2} c_{xxxx} (\varepsilon_{xx}^2 + \varepsilon_{yy}^2) + c_{xyxy} (\varepsilon_{xx} \varepsilon_{yy}) + c_{xxzz} (\varepsilon_{xx} + \varepsilon_{yy}) \varepsilon_{zz} \\ & + \frac{1}{2} c_{zzzz} \varepsilon_{zz}^2 + 2c_{yzyz} (\varepsilon_{yz}^2 + \varepsilon_{zx}^2) + 2c_{xyxy} \varepsilon_{xy}, \end{aligned}$$

where C_{ij} resp. c_{ijkl} denotes 6 independent elastic constants. E_0 and V_0 stand for the equilibrium energy and volume.

On the other hand, the magnetoelastic energy possessing in the tetragonal (I) case 7 independent magneto-

elastic constants b_i [17, 18] reads

$$\begin{aligned} \frac{1}{V_0} E_{me} = & b_{11} (\varepsilon_{xx} + \varepsilon_{yy}) + b_{12} \varepsilon_{zz} \quad (5) \\ & + b_{21} (\alpha_z^2 - \frac{1}{3}) (\varepsilon_{xx} + \varepsilon_{yy}) + b_{22} (\alpha_z^2 - \frac{1}{3}) \varepsilon_{zz} \\ & + \frac{1}{2} b_3 (\alpha_x^2 - \alpha_y^2) (\varepsilon_{xx} + \varepsilon_{yy}) + 2b'_3 \alpha_x \alpha_y \varepsilon_{xy} \\ & + 2b_4 (\alpha_x \alpha_z \varepsilon_{xz} + \alpha_y \alpha_z \varepsilon_{yz}). \end{aligned}$$

The first line describe the isotropic volume effect with coefficients b_{11} and b_{12} . The other lines are related to the anisotropic behavior.

Performing the energy minimization, the relative length change at the equilibrium strain in the tetragonal (I) system follows [12]

$$\begin{aligned} \frac{\Delta l}{l_0} \Big|_{\boldsymbol{\beta}}^{\boldsymbol{\alpha}} = & \lambda^{\alpha 1,0} (\beta_x^2 + \beta_y^2) + \lambda^{\alpha 2,0} \beta_z^2 \quad (6) \\ & + \lambda^{\alpha 1,2} (\alpha_z^2 - \frac{1}{3}) (\beta_x^2 + \beta_y^2) + \lambda^{\alpha 2,2} (\alpha_z^2 - \frac{1}{3}) \beta_z^2 \\ & + \frac{1}{2} \lambda^{\gamma,2} (\alpha_z^2 - \alpha_y^2) (\beta_x^2 - \beta_y^2) + 2\lambda^{\delta,2} \alpha_x \alpha_y \beta_x \beta_y \\ & + 2\lambda^{\varepsilon,2} (\alpha_x \alpha_z \beta_x \beta_z + \alpha_y \alpha_z \beta_y \beta_z), \end{aligned}$$

where the isotropic magnetostrictive coefficients describing the volume magnetostriction reads

$$\lambda^{\alpha 1,0} = \frac{b_{11} C_{33} + b_{12} C_{13}}{C_{33} (C_{11} + C_{12}) - 2C_{13}^2}, \quad (7)$$

$$\lambda^{\alpha 1,0} = \frac{2b_{11} C_{13} - b_{12} (C_{11} - C_{12})}{C_{33} (C_{11} + C_{12}) - 2C_{13}^2}. \quad (8)$$

Whereas the magnetization direction dependent relative length change (Eq. 6) is given by anisotropic coefficients

$$\lambda^{\alpha 1,2} = \frac{-b_{21} C_{33} + b_{22} C_{13}}{C_{33} (C_{11} + C_{12}) - 2C_{13}^2} \quad (9)$$

$$\lambda^{\alpha 2,2} = \frac{2b_{21} C_{13} - b_{22} (C_{11} + C_{12})}{C_{33} (C_{11} + C_{12}) - 2C_{13}^2} \quad (10)$$

$$\lambda^{\gamma,2} = \frac{-b_3}{C_{11} - C_{12}} \quad (11)$$

$$\lambda^{\delta,2} = \frac{-b'_3}{2C_{66}} \quad (12)$$

$$\lambda^{\varepsilon,2} = \frac{-b_4}{2C_{44}}. \quad (13)$$

Employing the MAELAS package [19], the above-mentioned anisotropic magnetoelastic b_i constants resp.

magnetostrictive coefficients λ_i can be easily evaluated using a finite displacement approach.

To obtain the fractional volume change,

$$\omega_S = \frac{\delta V}{V} = \varepsilon_{xx} + \varepsilon_{yy} + \varepsilon_{zz}, \quad (14)$$

we minimize the magneto-volume and elastic energy contributions with the respect to the strain [1].

Regarding the magneto-volume energy, the change in the energy for a pair of interacting spins along direction cosines $(\beta_x, \beta_y, \beta_z)$ with the respect to the strain reads [1]

$$\Delta E = \pm \frac{\partial J}{\partial r} \Big|_{r_0} r_0 \left(\varepsilon_{xx} \beta_x^2 + \varepsilon_{yy} \beta_y^2 + \varepsilon_{zz} \beta_z^2 + \varepsilon_{xy} \beta_x \beta_y + \varepsilon_{yz} \beta_y \beta_z + \varepsilon_{zx} \beta_z \beta_x \right), \quad (15)$$

where J denotes magnetic exchange interaction, plus sign is related to parallel (ferromagnetic) spin orientation, whereas the minus one for the anti-parallel (anti-ferromagnetic) orientation.

Calculating the magneto-volume energy (Eq. 15) for the tetragonal MnPt system, the contribution from the basal plane, related to the nearest neighbor interaction J_1 , reads

$$E_1^{\text{magvol}} = \pm 2 \frac{\partial J_1}{\partial r} r_1 (\varepsilon_{xx} + \varepsilon_{yy}) = \pm \frac{M_1}{V} (\varepsilon_{xx} + \varepsilon_{yy}), \quad (16)$$

where axes of the primitive MnPt cell are considered for simplicity (Fig. 2 - FM structure). Along the c -axis the next-nearest interactions J_2 contributes

$$E_2^{\text{magvol}} = \pm 2 \frac{\partial J_2}{\partial r} r_2 \varepsilon_{zz} = \pm \frac{M_2}{V} \varepsilon_{zz}. \quad (17)$$

In addition, J_3 and J_4 contributions are assumed. J_3 interactions points along $[110], [1\bar{1}0], [\bar{1}10], [\bar{1}\bar{1}0]$ directions with the respect to the MnPt primitive cell, where its total energy contribution read

$$\begin{aligned} E_3^{\text{magvol}} &= \pm \frac{\partial J_3}{\partial r} r_3 \\ &\times \left[\frac{1}{2} (\varepsilon_{xx} + \varepsilon_{yy} + \varepsilon_{xy}) + \frac{1}{2} (\varepsilon_{xx} + \varepsilon_{yy} - \varepsilon_{xy}) \right. \\ &\left. + \frac{1}{2} (\varepsilon_{xx} + \varepsilon_{yy} + \varepsilon_{xy}) + \frac{1}{2} (\varepsilon_{xx} + \varepsilon_{yy} - \varepsilon_{xy}) \right] \\ &= \pm 2 \frac{\partial J_3}{\partial r} r_3 (\varepsilon_{xx} + \varepsilon_{yy}) = \pm \frac{M_3}{V} (\varepsilon_{xx} + \varepsilon_{yy}). \end{aligned} \quad (18)$$

Regarding J_4 contribution, the interactions are in directions $[101], [\bar{1}01], [011], [0\bar{1}1], [10\bar{1}], [\bar{1}0\bar{1}], [01\bar{1}], [0\bar{1}\bar{1}]$ giving a following energy contribution

$$\begin{aligned} E_4^{\text{magvol}} &= \pm \frac{\partial J_4}{\partial r} r_4 \frac{4\varepsilon_{xx} + 4\varepsilon_{yy} + 8\left(\frac{c}{a}\right)^2 \varepsilon_{zz}}{\sqrt{1 + \left(\frac{c}{a}\right)^2}} \\ &= \pm \frac{4}{\sqrt{1 + \left(\frac{c}{a}\right)^2}} \frac{\partial J_4}{\partial r} r_4 \left[\varepsilon_{xx} + \varepsilon_{yy} + 2\left(\frac{c}{a}\right)^2 \varepsilon_{zz} \right] \\ &= \pm \frac{M_4}{V} \left[\varepsilon_{xx} + \varepsilon_{yy} + 2\left(\frac{c}{a}\right)^2 \varepsilon_{zz} \right]. \end{aligned} \quad (19)$$

Minimizing the sum of the magneto-volume and elastic energy with the respect to the strain, one obtains following relations

$$\frac{1}{V} \frac{\partial E}{\partial \varepsilon_{xx}} = \mathcal{A} + C_{11} \varepsilon_{xx} + C_{12} \varepsilon_{yy} + C_{13} \varepsilon_{zz} = 0, \quad (20)$$

$$\frac{1}{V} \frac{\partial E}{\partial \varepsilon_{yy}} = \mathcal{A} + C_{12} \varepsilon_{xx} + C_{11} \varepsilon_{yy} + C_{13} \varepsilon_{zz} = 0, \quad (21)$$

$$\frac{1}{V} \frac{\partial E}{\partial \varepsilon_{zz}} = \mathcal{B} + C_{13} \varepsilon_{xx} + C_{13} \varepsilon_{yy} + C_{33} \varepsilon_{zz} = 0. \quad (22)$$

Derived volume magnetostrictions ω_s in the case of the tetragonal (I) system then reads

$$\begin{aligned} \frac{\delta V}{V} = \omega_s &= \varepsilon_{xx} + \varepsilon_{yy} + \varepsilon_{zz} = \\ &\frac{2\mathcal{A}(C_{13} - C_{33}) + \mathcal{B}(2C_{13} - C_{11} - C_{12})}{C_{33}(C_{11} + C_{12}) - 2C_{13}^2}, \end{aligned} \quad (23)$$

where the \mathcal{A} and \mathcal{B} depends on the number of included nearest neighbor interactions. Assuming only the J_1 and J_2 interactions' contributions, the parameters read

$$\mathcal{A}V = M_1 = 2 \frac{\partial J_1}{\partial r} r_1 \quad (24)$$

$$\mathcal{B}V = M_2 = 2 \frac{\partial J_2}{\partial r} r_2. \quad (25)$$

Considering the interactions up to J_4 , the expressions change as follows

$$\begin{aligned} \mathcal{A}V &= M_1 + M_3 + M_4 \\ &= 2 \frac{\partial J_1}{\partial r} r_1 + 2 \frac{\partial J_3}{\partial r} r_3 + \frac{4}{\sqrt{1 + \left(\frac{c}{a}\right)^2}} \frac{\partial J_4}{\partial r} r_4, \end{aligned} \quad (26)$$

$$\begin{aligned} \mathcal{B}V &= M_2 + 2\left(\frac{c}{a}\right)^2 M_4 \\ &= 2 \frac{\partial J_2}{\partial r} r_2 + \frac{8}{\sqrt{1 + \left(\frac{c}{a}\right)^2}} \left(\frac{c}{a}\right)^2 \frac{\partial J_4}{\partial r} r_4. \end{aligned} \quad (27)$$

Alternatively, the $\frac{1}{V} \frac{\partial E^{\text{magvol}}}{\partial \varepsilon_{ii}}$ terms represented by \mathcal{A} resp. \mathcal{B} parameters (Eq. 23) can be obtained directly by calculating a strain dependence of exchange interactions J_{ij} , while the sign of the orientation of interacting moments is considered (Eq. 15).

The isotropic magnetic exchange interactions J_{ij} were evaluated by the fully relativistic version of the LKAG method based on the magnetic force theorem [20]. The interaction Hamiltonian reads

$$\hat{H} = - \sum_{i \neq j} \sum_{\{\alpha, \beta\} = \{x, y, z\}} e_i^\alpha \hat{J}_{ij}^{\alpha\beta} e_j^\beta, \quad (28)$$

where $\hat{J}_{ij}^{\alpha\beta}$ is a (3×3) interaction coupling tensor and e_i^α denotes spin components of unitary spin vector at the site i . However, here, only the isotropic Heisenberg

interaction J_{ij} is assumed, which is given as follows [20]

$$\hat{H} = - \sum_{i \neq j} J_{ij} \mathbf{e}_i \cdot \mathbf{e}_j, \quad (29)$$

$$J_{ij} = \frac{1}{3} \text{Tr} \hat{J}_{ij}^{\alpha\beta}. \quad (30)$$

So far, the magnetostrictive properties of the single crystalline samples have been discussed. Regarding a polycrystal, the averaged fractional length change between an initial state and saturated final state follows a relation

$$\left\langle \frac{l - l_0}{l} \right\rangle_{\beta}^{\alpha} = \xi + \eta(\boldsymbol{\alpha} \cdot \boldsymbol{\beta}), \quad (31)$$

where the form of ξ , η parameters depends on the initial demagnetized state [19].

Considering an initial state with randomly oriented atomic magnetic moments, the parameters reads

$$\xi = \frac{2}{3} \lambda^{\alpha 1,0} + \frac{1}{3} \lambda^{\alpha 2,0} + \frac{2}{45} \lambda^{\alpha 1,2} - \frac{2}{45} \lambda^{\alpha 2,2} - \frac{2}{15} \lambda^{\epsilon,2} - \frac{1}{15} \lambda^{\gamma,2} - \frac{1}{15} \lambda^{\delta,2} \quad (32)$$

$$\eta = -\frac{2}{15} \lambda^{\alpha 1,2} + \frac{2}{15} \lambda^{\alpha 2,2} + \frac{2}{5} \lambda^{\epsilon,2} + \frac{1}{5} \lambda^{\gamma,2} + \frac{1}{5} \lambda^{\delta,2} \quad (33)$$

. Whereas for an initial state with domains aligned along easy direction the ξ parameter is given

$$\xi = \frac{4}{15} \lambda^{\alpha 1,2} + \frac{1}{15} \lambda^{\alpha 2,2} - \frac{2}{15} \lambda^{\epsilon,2} - \frac{1}{15} \lambda^{\gamma,2} - \frac{1}{15} \lambda^{\delta,2} - \frac{1}{3} (2\lambda^{\alpha 1,2} + \lambda^{\alpha 2,2}) \cos^2 \theta, \quad (34)$$

where $\theta = 0$ for easy axis resp. $\theta = \frac{\pi}{2}$ for easy plane system. The η remains unchanged.

III. EXPERIMENT DETAILS

The polycrystalline sample of MnPt was prepared using an arc melting process with the MAM-1 system (Edmund Bühler GmbH). Stoichiometric amounts of high-purity manganese (99.9%) and platinum (99.99%) were melted under a titanium-gettered argon atmosphere. To ensure homogeneity, the sample was flipped and remelted multiple times. The final sample weighed approximately 1 g, with a mass loss of less than 0.5%. No further heat treatment was applied. X-ray diffraction (XRD) measurements were conducted at room temperature on a sample that had been hand-ground. These measurements were performed using a PANalytical X'pert Pro diffractometer, employing $\text{CuK}\alpha$ radiation produced at 40 kV and 30 mA ($\lambda = 1.5406 \text{ \AA}$) in a Bragg-Brentano geometry. The resulting XRD pattern was analyzed using FullProf software [21]. High-resolution magnetostriction measurements, tracking length changes as a function of

magnetic field (magnetostriction), were performed using a miniature capacitance dilatometer [22]. The dilatometer was connected to an AH2500A capacitance bridge, integrated into a Physical Property Measurement System (PPMS) from Quantum Design.

IV. CALCULATION DETAILS

The electronic structure calculations were performed within the plane-wave based Vienna ab-initio simulation package (VASP) [23, 24] employing the projector-augmented-wave (PAW) method with PAW pseudo-potentials. The calculation considers the generalized gradient approximation (GGA) of Perdew-Burke-Ernzerhof (PBE) [25]. In calculation, the non-collinear magnetism and spin-orbit coupling were considered. Energy cut-off (ENCUT) for the plane waves of 450 eV was used. In general, an automatic generation of k -mesh scheme with $R_k = 70$ was considered. Structure relaxation was performed on the relevant k -mesh, where the shown structure parameters are related to our default $R_k = 70$. The relaxation was performed by Methfessel-Paxton scheme of the order 1 with the smearing 0.01 eV. Due to the computation demands, the same was used, when R_k exceed 100. Elsewhere, the tetrahedron method with Blöchl corrections was employed. The energy convergence in structure relaxation calculations includes the convergence of the self-consistent loop better the EDIFF = 10^{-7} eV and energy difference between relaxation steps smaller the EDIFF = 10^{-6} eV. Regarding the calculation of the magnetoelastic properties and MAE a tight convergence was demanded EDIFF = 10^{-9} eV. To obtain a good linear fit of magnetoelastic constants b_i , $R_k = 120$ resp. $R_k = 110$ was used for the calculations of elastic and magnetoelastic properties in case of AFM1 resp. AFM2 magnetic structures. The elastic and magnetoelastic parameters were evaluated within AELAS [16] resp. MEALAS [12, 19] packages were used serving to generation of distorted structure and result analysis.

The applied strain in the magnetoelastic calculation differs between magnetic structures depending on the linearity of the obtained dependencies. In case of the FM structure, the maximum applied strain ε was 0.0075. AFM1 system showed linear behavior in a smaller region, and the maximal strain was reduced to 0.0050. Whereas for the AFM2 structure, the maximum strain 0.0100 can be applied except for the calculation of the b_2 parameter requiring reduction to 0.0075. The R-factor of the linear fitting was better 0.98 except for certain cases of low b values given by related extreme demands on precision.

MEA was estimated at a fine k -mesh (FM: $R_k = 75$, AFM: $R_k = 90$ and AFM2: $R_k = 95$) with tight energy convergence EDIFF = 10^{-8} eV. High accuracy calculations were needed to obtained smooth energy curves particularly for antiferromagnetic structures.

The exchange interaction parameters were calculated within the Relativistic Spin Polarized toolkit (RSPT)

package based on the Full-Potential Linear Muffin-Tin Orbital (FP-LMTO) method. The calculations were performed on $20 \times 20 \times 20$ k -mesh in the fully relativistic scheme, considering the xc-potential of PBE 96 and Perdew Wang 1992. Relaxed VASP crystal structures were used in the calculations. The energy convergence was better than 10^{-10} Ry and s,p,d orbitals were considered in the evaluation of exchange interactions.

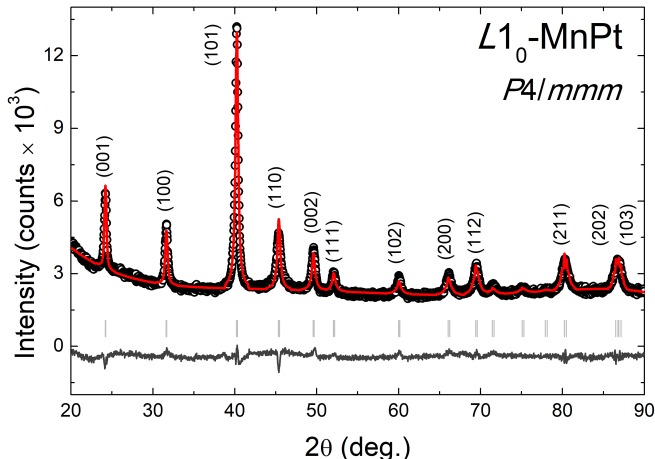


FIG. 1. The room temperature X-ray diffraction pattern for the MnPt sample. The open circles represent the experimental data, while the solid lines depict the Rietveld-refined pattern obtained using Fullprof software. The difference pattern is illustrated by the solid line at the bottom. Ticks indicate the positions of the Bragg reflections corresponding to the tetragonal CuAu-I type structure (space group $P4/mmm$, No. 123). The most prominent peaks are labeled with their Miller (hkl) indices.

V. RESULTS

A. Magnetic structures

Despite the experimentally reported antiferromagnetic ground state of the studied MnPt system [26], we also

TABLE I. Calculated MnPt magnetic structure energy differences and related structure parameters together with XRD refined data of the prepared sample. The structure data are shown according to the FM primitive cell except the a_{nr} denoting the basal edge in the non-reduced cell with 4 atoms in the basis.

	$\Delta E/f.u.$ (eV)	a (Å)	c (Å)	c/a	V (Å ³)	c/a_{nr}
NM	0.00	2.642	3.770	1.43	26.3	1.01
FM	-1.02	2.931	3.507	1.20	30.1	0.85
AFM1	-1.32	2.799	3.718	1.33	29.1	0.94
AFM2	-1.05	2.861	3.645	1.27	29.8	0.90
exp.		2.827	3.676	1.30	29.4	0.92

considered other magnetic structures [27, 28] to inspect the influence of the magnetic structure on the magnetoelastic behavior. Actually, we considered three collinear structures with magnetic moments pointing along the c -axis: ferromagnetic (FM) and two antiferromagnetic (AFM1, AFM2) structures (Fig. 2). In addition, non-magnetic (NM) system was considered as a reference state where applicable. Corresponding to the literature [26–29], the AFM1 state, with AFM ordered nearest-neighbor spins in the basal ab -plane, was found as the ground state (Table I). However, it has to note that the FM phase was observed in quenched powders and sputtered films of disordered MnPt [30]. The obtained energy differences are in agreement with the published ones [27, 28] as well as the relaxed structure parameters [28, 29, 31, 32]. Also, the estimated magnitudes of spin magnetic moments correspond to the literature [28, 29, 31]. Similarly to the FePt system, the Pt sublattices bear no magnetic moments except the FM phase [28]. Only the Mn atoms are magnetic, which can facilitate understanding of the magnetic behavior. Particularly, non-zero AFM oriented moments would break the tetragonal symmetry of the AFM1 structure in the ab -direction.

In addition, the density of the states (DOS) for the magnetic systems were compared (Fig. 3). According to the literature, a formation of a pseudo-gap for the AFM1 ground state was observed. It is assumed that the suppressed DOS around the Fermi level, pseudogap formation, is attributed to an antiferromagnetic staggered field [9]. Alike behavior does not occur for the FM and AFM2 structures. Particularly, AFM2 possesses a high DOS. It points out significant differences in the electronic structures between the AFM structures given by different orientations of the antiferromagnetic ordering. Nevertheless, for all the magnetic structures, the intensity of the Mn and Pt states is similar below the Fermi level, as the Pt conduction d-states spread across more than 6 eV while the Mn d-states tend to the Fermi level. Above, Mn dominates the conduction states for the studied energy range.

To validate the performed calculations, experimental results were obtained. Prior to the magnetostriction measurements, the crystal structure was also explored. XRD analysis indicated that the material crystallizes in a tetragonal CuAu-I type structure (space group $P4/mmm$, No. 123) (Fig. 1). The determined values of the lattice parameters are $a = 2.8267(2)$ Å and $c = 3.6755(3)$ Å, and are in good agreement with the literature data [33] and calculated AFM1 ground state, where the difference is about 1%.

B. Elastic behavior

The determination of magnetoelastic parameters requires knowledge of elastic coefficients C_{ij} . Since we occupy in this work not only with the ground state AFM1

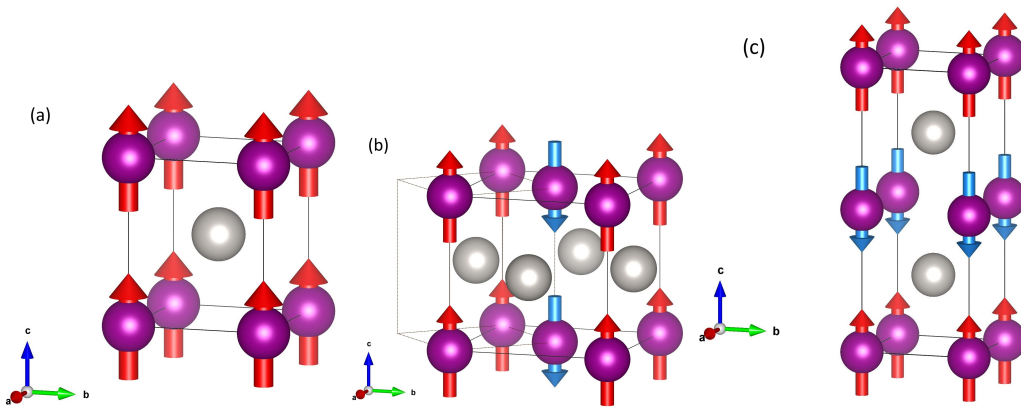


FIG. 2. MnPt Magnetic structures. (a) FM, (b) AFM1, (c) AFM2. Dashed lines in the AFM1 structure denote the primitive cell similar to the FM one.

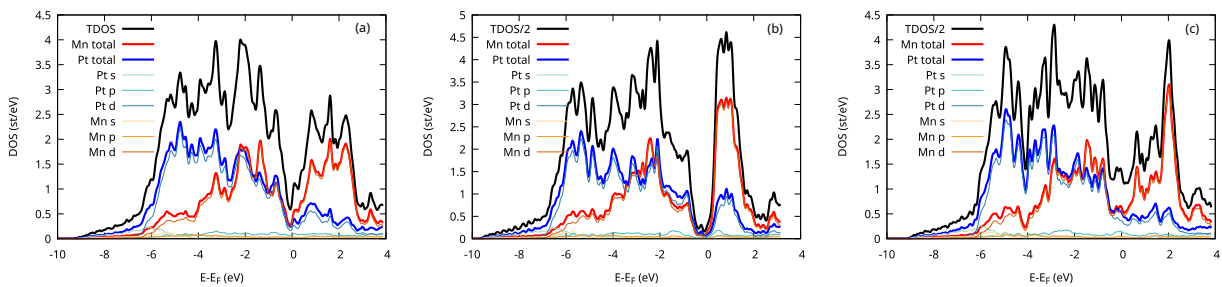


FIG. 3. Density of states with the respect to the magnetic structure. (a) FM, (b) AFM1, (c) AFM2.

magnetic structure but also the FM and AFM2. Elastic coefficients were estimated in all cases including the NM state for comparison. To be able to compare the results (Table III), the C_{ij} are defined with respect to the axes of the FM primitive cell. It means a rotation of the AFM1 cell and related coefficients in the ab -plane by 45 degrees. The elastic properties were evaluated by means of the final displacement method. Therefore, we checked whether displacement modified the magnetic structure as Pt magnetic moments in the AFM structure might be induced. However, no significant Pt moment was induced. It means that tetragonal symmetry can be safely applied

TABLE II. MnPt spin and orbital magnetic moment components with the respect to magnetic structure

	$\mu_{\text{Mn}}^{\text{L}} (\mu_{\text{B}})$			$\mu_{\text{Pt}}^{\text{L}} (\mu_{\text{B}})$		
	x	y	z	x	y	z
FM	0.00	0.00	0.03	0.00	0.00	0.07
AFM1	0.00	0.00	0.04	0.00	0.00	0.00
AFM2	0.00	0.00	0.03	0.00	0.00	0.00
	$\mu_{\text{Mn}}^{\text{S}} (\mu_{\text{B}})$			$\mu_{\text{Pt}}^{\text{S}} (\mu_{\text{B}})$		
	x	y	z	x	y	z
FM	0.00	0.00	3.82	0.00	0.00	0.37
AFM1	0.00	0.00	3.64	0.00	0.00	0.00
AFM2	0.00	0.00	3.76	0.00	0.00	0.00

in the case of the AFM1 system, as Pt moments are not induced by deformations. We verified it by evaluation of the elastic coefficients in both tetragonal ($Pmmm$) and orthorhombic ($P4/mmm$) symmetry, where identical values are obtained. (Table III).

The determined C_{ij} constants corresponds well to the published one (NM [31], AFM1 [34]), where we note that proper reference axes have to be chosen.

According to the calculated values, all the structures fulfilled *Born stability criteria* for tetragonal (I) sys-

TABLE III. MnPt elastic constants, In case of the the AFM1 structure, the C_{ij} constants were calculate with both tetragonal (t) and orthorhombic (o) symmetry consideration. Last column, show the AFM1 elastic constants with the respect to the axis of the non-reduced AFM1 cell (nr), for better comparison with the published data. Regarding the later case only certain parameters are shown.

C_{ij} (GPa)	NM	FM	AFM1 ^(t,o)	AFM2	AFM1 ^{nr}
C_{11}	549	252	306	238	258
C_{12}	109	87	72	82	120
C_{13}	171	152	141	155	141
C_{33}	424	224	284	220	284
C_{44}	195	99	123	87	123
C_{66}	115	69	69	48	117

tems [35, 36]: $C_{ii} > 0$; $C_{11} > |C_{12}|$; $2C_{13}^2 < C_{33}(C_{11} + C_{12})$. It means that the systems are stable at least at the Γ -point regarding the phonon spectra.

Based on the values, the NM structure has the highest bulk modulus, making the structure the most toughest. It is related to the smallest volume. The bulk modulus of the other magnetic ones is alike, corresponding to the similar volume, particularly of FM and AFM2 possessing comparable C_{ij} .

C. Magnetoelastic behavior

Having obtained the elastic constants, one can discuss the magnetoelastic constants b_i and magnetostrictive coefficients λ_i . The magnetoelastic constants arise from the change of MAE with respect to the applied strain and defined spin directions (Fig. 5). Thanks to much smaller energy differences with respect to the elastic constants (C_{ij} in order of GPa vs. b in MPa), highly accurate calculations are inevitable, as mentioned in the Methods section. Due to tiny lattice displacements enforced by required linearity, energy differences can be in the order of μeV for certain AFM b_i constants. The type of magnetic order substantially influences the MAE (Fig. 4) and therefore also the magnitudes of the b_i parameters including their signs, as demonstrates the estimated values of the magnetoelastic constants b_i (Table IV). For clarity, the values of b_i constants in Table IV are referred to the axis of the FM structure similarly to the previous case of the elastic constants (Table III). Table IV. One can notice that the b_i constants differ significantly, except the b'_3 one. Differences in the slopes of the MEA difference with respect to the applied strain, which is the meaning of the b_i constants, can be understood starting from differences in spin structure in relation to the magnetization axes directions or more rigorously by induced charge density differences regarding the applied deformations.

Starting from the b_{21} constant, the area of the ab -base is changed (Fig. 5). Regarding MnPt, it means that c/a ratio gets closer to 1 and the MAE for the defined magnetization directions α_1 and α_2 should be smaller by simple consideration. It agrees with the positive b_1 sign, except AFM2 case, as the difference $E_{\alpha_1} - E_{\alpha_2}$ is less negative. Concerning AFM2 and the minus sign, simply based

TABLE IV. MnPt magnetoelastic constants, Axes are oriented according the FM primitive cell, i.e. the AFM 1 structure is rotated about 45 deg along the c -axis to be able compare the results.

b (MPa)	FM	AFM1	AFM2
b_{21}	135	23	-62
b_{22}	-111	-38	23
b_3	-40	-73	118
b_4	-34	3	26
b'_3	86	94	75

on the spin orientations one finds that both in the FM and AFM case the spins along the magnetization axes α_1 resp. α_2 have the same direction, whereas for AFM2 it changes. Better explanation can provide changes in the charge density induced by the change of the magnetization axis, which were obtained by self-consistent calculations (Fig. 5).

Regarding the AFM2 magnetic structure, significant positive charge difference $\Delta\rho = \rho(\alpha_1) - \rho(\alpha_2)$ (Fig. 5) - yellow color) appears along a and b directions between Mn resp. particularly Pt atoms. Enlarging the a parameter, the related extra energy contribution for the α_1 magnetization direction can be reduced, which can lower the E_{α_1} with the respect to E_{α_2} . The nearest Mn-Pt distance is shorter than the a parameter, so the effect might be more important. However, the change of the charge density has no dominating character in this direction. On the other hand, a quite opposite character of the charge density differences for the FM magnetic structure was calculated. It agrees with the opposite sign of the b_{21} sign. Finally, the AFM1 charge difference does not offer an easily visible preference either for α_1 resp. α_2 magnetization direction, which might explain the small b_{21} constant. Its positive sign likely comes from a negative charge density difference along the Mn-Pt direction. The parts of charge density most probably contributing to b_i parameters are denoted in the Fig. 5.

Qualitatively, the high FM b_1 value can correspond to a strong magneto-crystalline anisotropy of FM structure compared to AFM ones (Fig. 4). The FM anisotropic constant K_1 is one resp. two orders of magnitude larger than AFM1 resp. AFM2 ones. Further, also K_2 constants differ significantly across the magnetic structures, being largest for AFM1 magnetic structure. Simply speaking, the K_1 dominates for FM state. However, it is comparable to AFM1 K_2 constant. Remarkably, the K_2 constant dominates the AFM2 state, making its behavior quite different. Besides, the K_3 constant is substantial in AFM states, while it is negligible for the FM state.

The b_{22} constant is related to the opposite behavior to the b_{21} as it comes from elongation of the c -axis (Fig. 5) likely followed by increasing of the MAE at least for the FM magnetic structure. Indeed, we observed almost opposite behavior both in the signs and magnitudes. Nevertheless, the different parts of the charge density likely contribute.

Analyzing the orbital origin of the MAE, the shape of the charge differences and its sign correspond to the orbital resolved MAE contributions (Fig. 6) obtained by summation of the lm-resolved band energies across the Brillouin zone. The lm-resolved energy of the ion i with magnetization axes α reads

$$E_{lm}^i(\alpha) = \sum_{n,\mathbf{k}} E_{n\mathbf{k}} |Y_{lm}^i|\phi_{n\mathbf{k}}|^2 c_{n\mathbf{k}}, \quad (35)$$

where the $E_{n\mathbf{k}}$ is the band energy of the band n at \mathbf{k} -point \mathbf{k} with occupancy $c_{n\mathbf{k}}$. Finally Y_{lm}^i denotes spherical harmonic centered at the ion i .

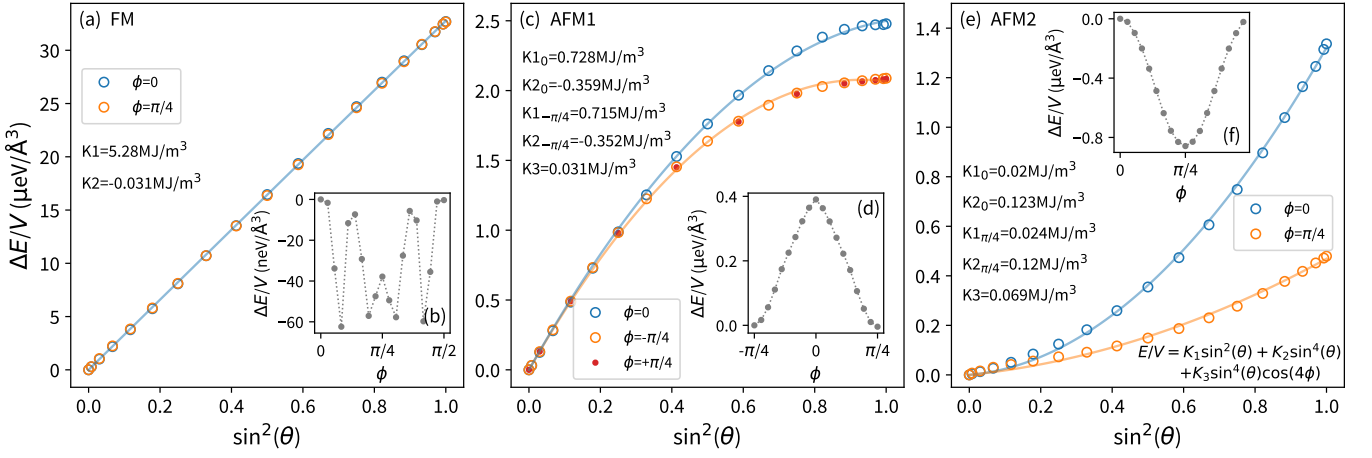


FIG. 4. Magneto-crystalline anisotropy. (a,b) FM, (c,d) AFM1, (e,f) AFM2 magnetic structures. The insets (b,d,f) denote a change of the MAE in the ab -plane. Regarding the AFM1 magnetic structure the axis orientation according to the FM structures are considered.

Regarding the FM structure, there is strong anisotropy coming from Pt d -orbitals. Nevertheless their contributions partly counteract. Besides, there are smaller contributions from Mn. Changing the magnetic structure, the Mn contribution dominates for AFM1 structure corresponding to the charge density differences (Fig. 5). The highlighted d_{xz} and d_{yz} orbitals (Fig. 6) are related to negative ρ which would explain positive b_{21} . The similar applies to b_{22} and d_{z^2} . Finally, Pt d_{z^2} and $d_{x^2-y^2}$ contributions seem to be the most important for the structure of AFM2, corresponding to $\Delta\rho$ (Fig. 5). Both the lm-resolved energy and charge density differences indicated that different orbitals are substantial depending on the magnetic structure, which likely lead to different b_i values. One has to point out, that the performed projections to the spherical harmonics are not complete. The summations of the occupancies over all projection does not yield proper number of electrons as around two electron charges are missing in general. Therefore, MAE even its lm contributions cannot be safely estimated from the lm energy projections.

So far, α_1 and α_2 yield non-zero MAE even without the applied strain. Concerning the other constants b_3 , b_4 and b'_3 , the MAE is enforced by strain. Regarding the b_3 one, where the shape of the ab -basis is changed, the FM and AFM1 states prefer magnetization axis along the elongated a axis, $E_{\alpha_1} - E_{\alpha_2}$ is negative. In the case of FM, it comes likely from the charge density differences between Mn and Pt (Fig. 5), see dominant energy lm-contributions of d_{xz} and d_{yz} (Fig. 6). For the AFM1, the situation is more complex as opposite spin appears within layer. Nevertheless, the mechanism can be similar to that in the FM case. The lm-resolved contributions do not help, since there are opposite lm-contributions which almost cancel out and the projections do not provide accurate information as mentioned above. The positive sign of the AFM2 b_3 coefficients can be attributed to strong Mn related charge density difference likely coming from

d_{xz} resp. d_{yz} behaving in the opposite way to FM state. Therefore, the magnetization alignment perpendicular to the elongation is preferred.

Further, b_4 coefficient is related to the modification of the ac -diagonal length. The FM state prefers moments align along the elongated diagonal, whereas the AFM states favor the antiparallel point along the shorter one (Fig. 5). The preference of the α_1 by FM states likely comes from d_{xz} states (Fig. 6) bringing the extra charge along the ca -diagonal. Particularly, the Mn contributions (Fig. 5) show slightly asymmetric behavior with the respect to magnetization directions. Concerning AFM states, $\Delta\rho$ clearly shows that α_1 brings extra density to the shrinking Mn-Pt direction, whereas for α_2 the density appears with the elongated direction, which should be preferred. Moreover, the b_4 constant magnitude grows with the $\Delta\rho$ prominence.

Finally, the b'_3 coefficients bear the similar behavior irrespective to the magnetic state (Table IV). All systems prefer parallel ordered spins along the squeezed ab -diagonal with similar b'_3 magnitude. The explanation is likely simple for the FM and AFM2 structures where α_2 axis reduces the charge density for shrinking Mn-Pt direction. Regarding the AFM1, the distributions of $\Delta\rho$ are quite complex, and hence it is not clear from which region the substantial interactions come.

For completeness, the AFM1 magnetoelastic constants were estimated with respect to the axes of non-reduced AFM1 cell (Table VI), meaning a $\pi/4$ rotation along the c -axis with the respect the above mentioned results (Table IV). Rotation of the a and b axes in the basal plane leads to a significant change of the b_i coefficients. The signs of b_{21} and b_{22} coefficients is kept, while their magnitude is reduced. One can relate it to the K_3 anisotropic constant and reduction of the MAE with the $\pi/4$ rotation (Fig. 4). Further, the change of the coordinates switch the sign of the b_3 and b'_3 coefficients related to the magnetization axes in the basal plane. Eventually, the b_4

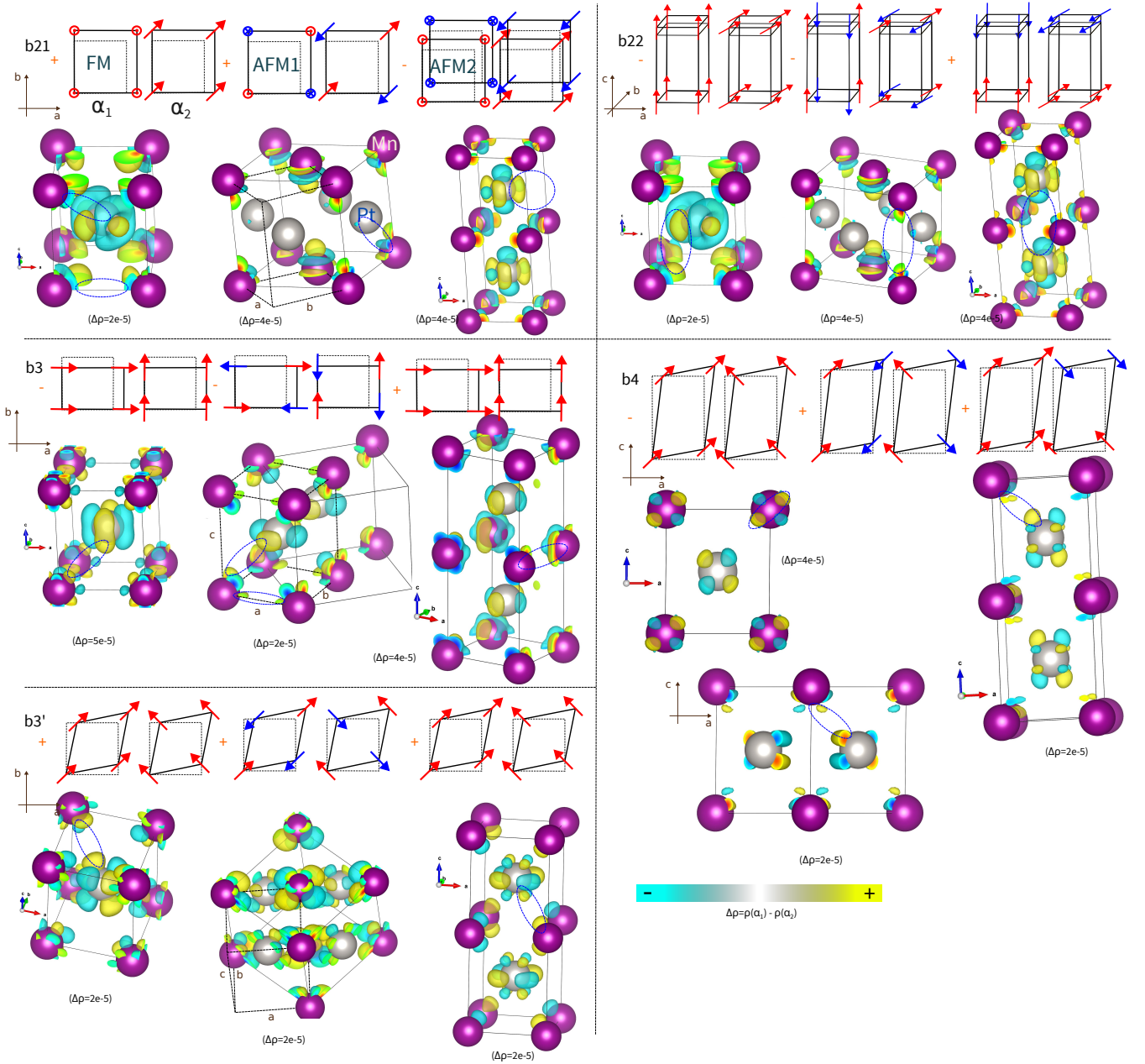


FIG. 5. Lattice deformations and spin directions related to calculation of magnetoelastic coefficients with related charge density differences. Considered FM, AFM1 and AFM2 magnetic structures with spin orientations are depicted. Charge density difference between the system with magnetization along α_1 and α_2 directions from self-consistent calculations are shown for each magnetic structure and type of deformation with the applied strain $\varepsilon=0.005$. Yellow color denotes charge density difference related to α_1 magnetization direction and cyan one to α_2 direction. Deformation with the respect to the FM axis are considered as in the Table IV. Below each charge density plot the magnitude of the plotted $\Delta\rho$ isosurface is stated.

becomes negligible. Therefore, it is important to choose the proper reference basis.

In addition, the magnetoelastic coefficients were obtained not only for the tetragonal symmetry but also for the orthorhombic one. It proves that the tetragonal symmetry considerations are valid for the AFM1 structure.

Nevertheless, more important from the experimental

point of view are the magnetostrictive coefficients λ^i (Table V) describing the change of length with respect to the sample magnetization (Eq. 2). Magnetic structure-dependent differences in the magnetoelastic constants b_i give rise to substantial differences in the magnetostrictive behavior. The most striking differences are in the magnitudes of the $\lambda^{\alpha_1,2}$ and $\lambda^{\alpha_2,2}$ constants coming from the

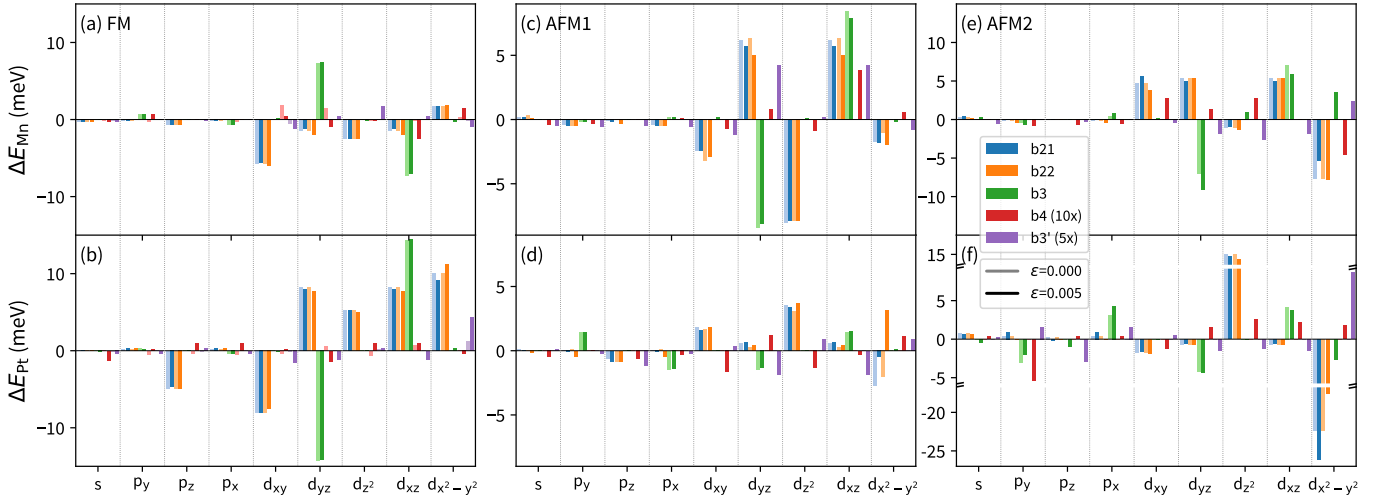


FIG. 6. Atomic orbital resolved energy contribution to MAE. (a,b) FM, (c,d) AFM1, (e,f) AFM2. The energy difference $\Delta E = E_{\alpha_2} - E_{\alpha_1}$ is related to magnetization axes shown in Fig. 5.

b_{21} and b_{22} magnetoelastic coefficients. The $\lambda^{\alpha 1,2}$ constant describes an enlargement of the ab -basis area for magnetization applied along the c -axis, whereas $\lambda^{\alpha 1,2}$ is related to the elongation of the c -parameter. Concerning the FM state, a huge ab -basis area squeezing compensated by enormous c -axis elongation was revealed. An opposite behavior of half-magnitude weaker was found for the AFM2. The opposite signs come from the magnetoelastic coefficient discussed above, where the differences in the behavior are described. They are also responsible for modest values related to the AFM1 structure, since the elastic constants are comparable between magnetic states. Found magnitudes of FM and AFM2 $\lambda^{\alpha 1,2}$ and $\lambda^{\alpha 2,2}$ coefficients are outstanding compared to other compounds [37].

The $\lambda^{\gamma,2}$ coefficient arising from b_3 constant denotes the change in length along the a resp. b axis with difference in the magnetization direction ($\alpha_x^2 - \alpha_y^2$) resp. ($\alpha_y^2 - \alpha_x^2$). Hence, it does not contribute when $\alpha_x^2 = \alpha_y^2$. Both FM and AFM1 states in the basal plane prefer the elongation along the basal magnetization. Behavior of the AFM2 is opposite and way stronger. The shear in the ab basis given by the inplane components of the magnetization axis is attributed to $\lambda^{\delta,2}$ coefficient. It

TABLE V. Magnetostrictive coefficients λ . Cell axes are oriented according the FM primitive cell due to a results comparison.

λ (10^{-6})	FM	AFM1	AFM2
$\lambda^{\alpha 1,2}$	-1592	-177	757
$\lambda^{\alpha 2,2}$	2655	310	-1168
$\lambda^{\gamma,2}$	240	312	-754
$\lambda^{\epsilon,2}$	170	-12	-151
$\lambda^{\delta,2}$	-620	-679	-775

is substantial irrespective of the magnetic order bearing similar values as b_3' hardly vary. On the other hand, the shear perpendicular to the ab basis related to $\lambda^{\epsilon,2}$ is much weaker. Particularly for the AFM1 state, the MAE is almost unchanged with deformation (b_4).

So far, the properties of the single-crystalline sample have been discussed. Nevertheless, even for polycrystals the averaged length fractional change can be evaluated. Particularly, an initial state with domains aligned along the easy axis (Fig. 4) was considered. Related parameters were calculated for all three magnetic structures. Moreover, for the AFM1 magnetic structure, the results obtained for different axes orientation were used. The results revealed a distinct behavior of particular magnetic structures. In the case of the FM state, the magnetization direction independent parameter ξ indicates slight shrinkage of the volume, which is overwhelmed by a nearly one order of magnitude larger elongation of the sample along the magnetization direction, thanks to the FM order. On the other hand, in the case of the AFM2

TABLE VI. Magnetoelastic constants and magnetostrictive coefficient for AFM1 with the natural non-reduced. Tetragonal and orthorhombic symmetry considered

tetragonal				orthorhombic			
b	(MPa)	λ	(10^{-6})	b	(MPa)	λ	(10^{-6})
b_{21}	9	$\lambda^{\alpha 1,2}$	-71	b_1	11	λ^1	-81
b_{22}	-15	$\lambda^{\alpha 2,2}$	126	b_2	-33	λ^2	232
b_3	43	$\lambda^{\gamma,2}$	-310	b_3	-33	λ^3	230
b_4	1	$\lambda^{\epsilon,2}$	-2	b_4	11	λ^4	-82
b_3'	-37	$\lambda^{\delta,2}$	158	b_5	14	λ^5	-122
				b_6	13	λ^6	-121
				b_7	-37	λ^7	154
				b_8	1	λ^8	-52
				b_9	1	λ^9	-52

system the sample volume tends to an expansion due to ξ while the length along the magnetization direction is reduced based on the η parameter. Still, the η parameter is much larger than the ξ one. Unlike the FM and AFM2 order, the system with the AFM1 type of magnetic ordering does not tend to such significant magnetostrictive effects, as the values of the ξ and η parameters are about one or two orders of magnitudes smaller. Interestingly, the parameters possess similar magnitudes. The calculations provide consistent results for different employed coordinate system and considered symmetries (Tables V and VI). The estimation of such tiny values requires extreme precision, still small differences occur. According to Eq. 34, the highest contribution to the ξ parameter comes from $\lambda^{\alpha 1,2}$ and $\lambda^{\alpha 2,2}$ coefficients giving terms with opposite signs irrespective of the magnetic state. Regarding the *eta* parameter, for the FM state the leading contributions are from $\lambda^{\alpha 1,2}$ and $\lambda^{\alpha 2,2}$ coefficients. However, the negative AFM1 *eta* parameter arise from $\lambda^{\delta,2}$ one. Finally, thanks to the signs of AFM2 λ_i parameters, all contributions sum up in a large negative AFM2 η value.

To validate the calculated results, we compared them with our measured magnetostiction data (Fig. 7). The measurements were performed with different mutual orientations of the length change and the applied external magnetic field. Considering Eq. 31, the curve measured for the external magnetic field perpendicular to the length change (Fig. 7 - blue curve) should be related to the ξ parameter. Then, the difference between the parallel and perpendicular field orientation is reflected by the η parameter (Table VII). The measured difference in magnetostriction for the parallel and perpendicular applied field is around -10^{-5} , which is consistent with the calculated values of the AFM1 ground state. The ξ parameters does not match properly to the experiment. However, one has to point out that we did not reach a saturated magnetization (Table VII - inset) in the experiments. Further, values of parameters strongly depend on the initial state of the experimental sample. Besides, one has to take into account tiny calculated values which meet the numerical precision of the calculations. Assuming the differences between the parameters obtained for various settings (Table VII), the difference with the experimental values is likely within the numerical error.

In the above, the anisotropic magnetoelastic properties were discussed. For a complete description, the isotropic volume change ω_s in case of the AFM1 structure was determined by minimizing the magneto-volume and elastic energy with respect to the strain based on the magnetic

TABLE VII. Magnetostriction of the prepared polycrystalline MnPt sample.

	FM	AFM1	AFM1 ^(t)	AFM1 ^(o)	AFM2
ξ (10^{-6})	-68	14	6	8	130
η (10^{-6})	558	-13	-5	-6	-623

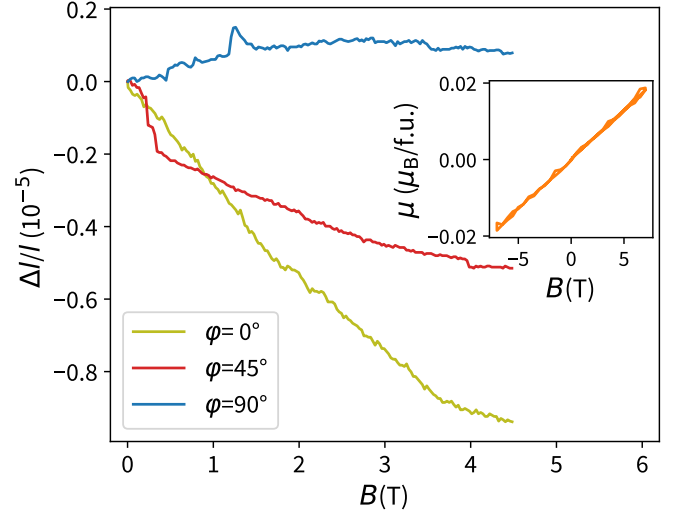


FIG. 7. Experimental MnPt magnetostriction. Magnetostriction was measured (olive) parallel, (blue) perpendicular and (red) in 45 deg to the applied magnetic field. The inset depicts the magnetization curve of the sample.

exchange interactions and elastic constants. The dependence of the magneto-volume energy was determined first by employing the radial dependence of the isotropic magnetic exchange coupling J_{ij} (Eq. 15) up to the J_4 interaction, where the calculated magnitudes of the exchange interactions agree to the literature [29]. The slopes $\partial J_i / \partial r$ were obtained by fitting the volume dependence of particular exchange interactions J_i (Fig. 8). Actually, small volume changes related to linear behavior were assumed, i.e. $|\Delta V| < 2\%$ except for J_3 where $|\Delta V| < 1\%$ was used.

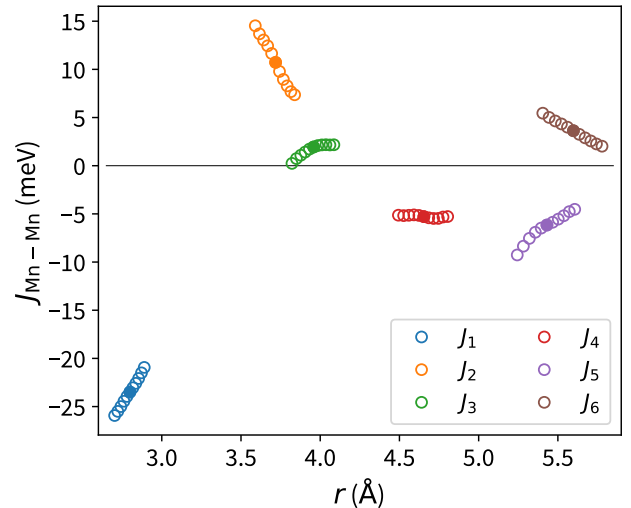


FIG. 8. Volume dependence of AFM1 magnetic exchange interactions. Filled circles denotes exchange interactions related to unchanged AFM1 volume V_0 (Table I). Depicted data are related to volume change between $0.9V_0$ and $1.1V_0$.

However, due to tetragonal symmetry, the mentioned

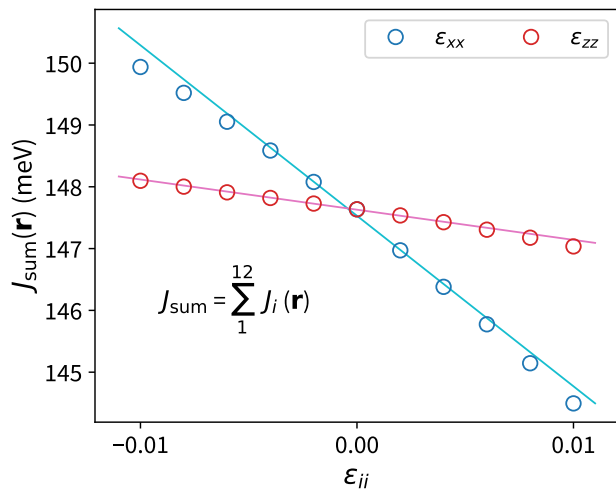


FIG. 9. Strain dependence of a sum of magnetic exchange interactions. (circles) Sum of the exchange interactions up to 12^{th} neighbor with respect to the unstrained system. (lines) Fitted slope in the vicinity of zero strain.

approach might fail as it does not distinguish between interactions within the basal plane and along the c -axis. The volume J_{ij} dependence approach is more appropriate for cubic systems. Thereby, the strain dependencies of the exchange interactions J_{ij}/ε_{ii} ($ii=\{xx, yy, zz\}$) were calculated (Fig. 9) allowing direct estimation of the \mathcal{A} (Eqs. 20 and 21) and \mathcal{B} (Eq. 22) parameters. To reach a linear behavior of the strain J_{ij} dependence (Fig. 9), only tiny stress was considered for linear fits, i.e. $|\varepsilon_{xx}|, |\varepsilon_{yy}| < 0.006$ mostly and $|\varepsilon_{zz}| < 0.004$. The ω_s values obtained by both approaches are of the same order (Fig. 10). However, their magnitudes start to differ when more distant neighboring interactions are considered (compare results up to J_2 vs up to J_4). The nearest-neighbor interactions can be used to rough estimate the ω_s . Nonetheless, a much more distant J_{ij} interactions seem to be assumed to reach a kind of convergence (Fig 10). Finally, we note that we did not used the unknown paramagnetic volume in Eqs. 20-22. Instead, the volume of the AFM1 phase was considered. However, due to a tiny ω_s value, the error is of the \mathcal{O}^3 order.

VI. CONCLUSIONS

In this work, we showed significant dependence of the magnetoelastic properties on the type of magnetic ordering. Regarding the antiferromagnetic ground state, the magnetoelastic effects are smaller. Likely, the strong magnetic coupling yielding high Neel temperature makes

the system insensitive to the applied field. However, for the ferromagnetic state detected in quenched powders and sputtered films, the magneto elastic response

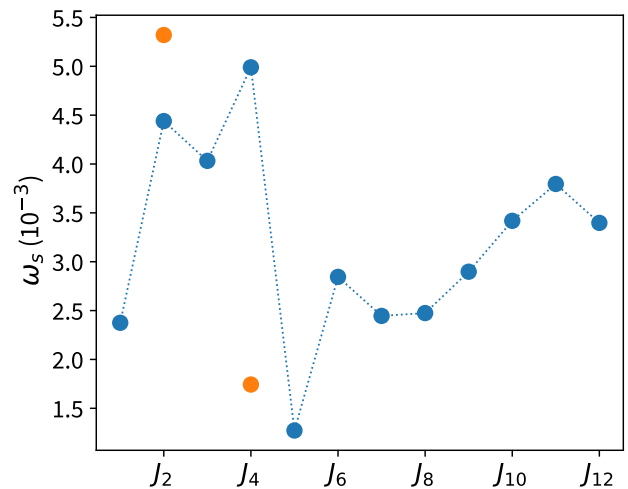


FIG. 10. Volume magnetostrictions ω_s . Dependence on the number of assumed interaction shells is provided. The values ω_s were determined either (orange points) based on the radial dependence $\partial J/\partial r$ or (blue points) employing the strain dependence $\partial J/\partial \varepsilon_{ii}$ ($ii=\{xx, yy, zz\}$) of the exchange interactions. X-labels denote the most distant pair exchange interaction with respect to non-deformed system assumed in the calculation.

is enormous, exceeding the effect in related FePt compound [37]. We probed the origin of the differences in the magnetoelastic behavior by analyzing charge differences and orbital-resolved MEA contributions. It revealed a significant difference in orbitals responsible for the magnetoelastic effects. The calculated results were supported by experimental measurements confirming the antiferromagnetic ground state properties including the magnetostrictive behavior. Finally, in addition to the anisotropic magnetoelastic parameters, the the isotropic volume change ω_s of the AFM1 magnetic state was estimated based on two approaches. A relatively slow convergence with respect to the assumed interaction shells indicates the importance of a more distant magnetic exchange.

VII. ACKNOWLEDGEMENTS

This work has been supported by GAČR project 24-11388I of the Grant Agency of Czech Republic and by the Ministry of Education, Youth and Sports of the Czech Republic through the e-INFRA CZ (ID:90254) and QM4ST project No. CZ.02.01.01/00/22.008/0004572.

- [1] S. Chikazumi, *Physics of Ferromagnetism*, International Series of Monographs on Physics (OUP Oxford, 2009).
- [2] N. Ekreem, A. Olabi, T. Prescott, A. Rafferty, and M. Hashmi, An overview of magnetostriction, its use and methods to measure these properties, *Journal of Materials Processing Technology* **191**, 96 (2007), advances in Materials and Processing Technologies, July 30th - August 3rd 2006, Las Vegas, Nevada.
- [3] B. Spetzler, C. Bald, P. Durdaut, J. Reermann, C. Kirchof, A. Teplyuk, D. Meyners, E. Quandt, M. Höft, G. Schmidt, and F. Faupel, Exchange biased delta-e effect enables the detection of low frequency pt magnetic fields with simultaneous localization, *Scientific Reports* **11**, 5269 (2021).
- [4] F. T. Calkins, A. B. Flatau, and M. J. Dapino, Overview of magnetostrictive sensor technology, *Journal of Intelligent Material Systems and Structures* **18**, 1057 (2007), <https://doi.org/10.1177/1045389X06072358>.
- [5] A. Bienkowski and R. Szewczyk, The possibility of utilizing the high permeability magnetic materials in construction of magnetoelastic stress and force sensors, *Sensors and Actuators A: Physical* **113**, 270 (2004), new materials and Technologies in Sensor Applications, Proceedings of the European Materials Research Society 2003 - Symposium N.
- [6] P. Kuszewski, I. S. Camara, N. Biarrotte, L. Becerra, J. von Bardeleben, W. Savero Torres, A. Lemaître, C. Gourdon, J.-Y. Duquesne, and L. Thevenard, Resonant magneto-acoustic switching: influence of rayleigh wave frequency and wavevector, *Journal of Physics: Condensed Matter* **30**, 244003 (2018).
- [7] P. Ravindran, A. Kjekshus, H. Fjellvåg, P. James, L. Nordström, B. Johansson, and O. Eriksson, Large magnetocrystalline anisotropy in bilayer transition metal phases from first-principles full-potential calculations, *Phys. Rev. B* **63**, 144409 (2001).
- [8] E. Krén, G. Kádár, L. Pál, J. Sólyom, P. Szabó, and T. Tarnóczy, Magnetic structures and exchange interactions in the mn-pt system, *Phys. Rev.* **171**, 574 (1968).
- [9] M. Kubota, K. Ono, R. Y. Umetsu, H. Akinaga, A. Sakuma, and K. Fukamichi, Pseudogap formation in mnpt and mnpd alloys, *Applied Physics Letters* **90**, 091911 (2007), https://pubs.aip.org/aip/apl/article-pdf/doi/10.1063/1.2561008/13159938/091911_1_online.pdf.
- [10] H. Hama, R. Motomura, T. Shinozaki, and Y. Tsunoda, Spin-flip transition of l10-type mnpt alloy single crystal studied by neutron scattering, *Journal of Physics: Condensed Matter* **19**, 176228 (2007).
- [11] L. Landau, L. Landau, E. Lifshits, A. Kosevich, E. Lifshitz, and L. Pitaevskii, *Theory of Elasticity: Volume 7*, Course of theoretical physics (Butterworth-Heinemann, 1986).
- [12] P. Nieves, S. Arapan, S. Zhang, A. Kadzielawa, R. Zhang, and D. Legut, Maelas: Magneto-elastic properties calculation via computational high-throughput approach, *Computer Physics Communications* **264**, 107964 (2021).
- [13] J. Cullen, A. Clark, and K. Hathaway, *Materials Science and Technology*, Vol. pp. 529 (VCH Publishings, 1994).
- [14] G. Engdahl and I. D. Mayergoyz, *Handbook of giant magnetostrictive materials*, Vol. 107 (Elsevier, 2000).
- [15] A. Clark, Chapter 7 magnetostrictive rare earth-fe2 compounds (Elsevier, 1980) pp. 531–589.
- [16] S. Zhang and R. Zhang, Aelas: Automatic elastic property derivations via high-throughput first-principles computation, *Computer Physics Communications* **220**, 403 (2017).
- [17] E. Callen and H. B. Callen, Magnetostriction, forced magnetostriction, and anomalous thermal expansion in ferromagnets, *Phys. Rev.* **139**, A455 (1965).
- [18] D. Fritsch and C. Ederer, First-principles calculation of magnetoelastic coefficients and magnetostriction in the spinel ferrites cofe_2o_4 and nife_2o_4 , *Phys. Rev. B* **86**, 014406 (2012).
- [19] P. Nieves, S. Arapan, S. Zhang, A. Kadzielawa, R. Zhang, and D. Legut, Maelas 2.0: A new version of a computer program for the calculation of magneto-elastic properties, *Computer Physics Communications* **271**, 108197 (2022).
- [20] A. Szilva, Y. Kvashnin, E. A. Stepanov, L. Nordström, O. Eriksson, A. I. Lichtenstein, and M. I. Katsnelson, Quantitative theory of magnetic interactions in solids, *Rev. Mod. Phys.* **95**, 035004 (2023).
- [21] J. Rodríguez-Carvajal, Recent advances in magnetic structure determination by neutron powder diffraction, *Physica B: Condensed Matter* **192**, 55 (1993).
- [22] M. Rotter, H. Müller, E. Gratz, M. Doerr, and M. Loewenhaupt, A miniature capacitance dilatometer for thermal expansion and magnetostriction, *Review of Scientific Instruments* **69**, 2742 (1998), https://pubs.aip.org/aip/rsi/article-pdf/69/7/2742/19318373/2742_1_online.pdf.
- [23] G. Kresse and J. Furthmüller, Efficient iterative schemes for ab initio total-energy calculations using a plane-wave basis set, *Phys. Rev. B* **54**, 11169 (1996).
- [24] G. Kresse and D. Joubert, From ultrasoft pseudopotentials to the projector augmented-wave method, *Phys. Rev. B* **59**, 1758 (1999).
- [25] J. P. Perdew, K. Burke, and M. Ernzerhof, Generalized gradient approximation made simple, *Phys. Rev. Lett.* **77**, 3865 (1996).
- [26] L. Pál, E. Krén, G. Kádár, P. Szabó, and T. Tarnóczy, Magnetic structures and phase transformations in mn-based cuau-i type alloys, *Journal of Applied Physics* **39**, 538 (1968), https://pubs.aip.org/aip/jap/article-pdf/39/2/538/18345168/538_1_online.pdf.
- [27] Q. ul ain, D. D. Cuong, D. Odkhuu, S. Rhim, and S. Hong, Thickness effect on magnetocrystalline anisotropy of mnpt(001) film, *Journal of Magnetism and Magnetic Materials* **467**, 69 (2018).
- [28] Z. Lu, R. V. Chepulskii, and W. H. Butler, First-principles study of magnetic properties of L1₀-ordered mnpt and fept alloys, *Phys. Rev. B* **81**, 094437 (2010).
- [29] K. Kang, D. G. Cahill, and A. Schleife, Phonon, electron, and magnon excitations in antiferromagnetic l1₀-type mnpt, *Phys. Rev. B* **107**, 064412 (2023).
- [30] C. S. Severin and C. W. Chen, Ferromagnetic behavior of disordered mnpt films produced by rf sputtering, *Journal of Applied Physics* **49**, 1693 (1978), https://pubs.aip.org/aip/jap/article-pdf/49/3/1693/18378964/1693_1_online.pdf.
- [31] J. Wang, A. Gao, W. Chen, X. Zhang, B. Zhou, and Z. Jiang, The structural, elastic, phonon, thermal and

- electronic properties of mnx ($x=ni, pd$ and pt) alloys: First-principles calculations, *Journal of Magnetism and Magnetic Materials* **333**, 93 (2013).
- [32] P. Ravindran, A. Kjekshus, H. Fjellvåg, P. James, L. Nordström, B. Johansson, and O. Eriksson, Large magnetocrystalline anisotropy in bilayer transition metal phases from first-principles full-potential calculations, *Phys. Rev. B* **63**, 144409 (2001).
- [33] R. M. A. F. Andresen, A. Kjekshus and W. B. Pearson, Equiatomic transition metal alloys of manganese iv. a neutron diffraction study of magnetic ordering in the $ptmn$ phase, *The Philosophical Magazine: A Journal of Theoretical Experimental and Applied Physics* **11**, 1245 (1965), <https://doi.org/10.1080/14786436508224933>.
- [34] D. Aissat, N. Baadji, H. Mazouz, and A. Boussendel, Connection between lattice parameters and magnetocrystalline anisotropy in the case of 110 ordered antiferromagnetic $mnpt$, *Journal of Magnetism and Magnetic Materials* **563**, 170013 (2022).
- [35] F. Mouhat and F. m. c.-X. Coudert, Necessary and sufficient elastic stability conditions in various crystal systems, *Phys. Rev. B* **90**, 224104 (2014).
- [36] D. Legut and J. Pavlů, Electronic structure and elasticity of z -phases in the $cr-nb-v-n$ system, *Journal of Physics: Condensed Matter* **24**, 195502 (2012).
- [37] D. Legut and P. Nieves, Second-order anisotropy due to magnetostriction for 110-fept, *Solid State Sciences* **160**, 107782 (2025).